

Large eddy simulation of a large wind-turbine array in a conventionally neutral atmospheric boundary layer

Dries Allaerts and Johan Meyers

Citation: *Physics of Fluids* **27**, 065108 (2015); doi: 10.1063/1.4922339

View online: <http://dx.doi.org/10.1063/1.4922339>

View Table of Contents: <http://scitation.aip.org/content/aip/journal/pof2/27/6?ver=pdfcov>

Published by the [AIP Publishing](#)

Articles you may be interested in

[Influence of atmospheric stability on wind-turbine wakes: A large-eddy simulation study](#)

Phys. Fluids **27**, 035104 (2015); 10.1063/1.4913695

[A stochastic perturbation method to generate inflow turbulence in large-eddy simulation models: Application to neutrally stratified atmospheric boundary layers](#)

Phys. Fluids **27**, 035102 (2015); 10.1063/1.4913572

[Large eddy simulation study of scalar transport in fully developed wind-turbine array boundary layers](#)

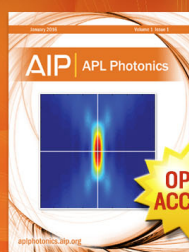
Phys. Fluids **23**, 126603 (2011); 10.1063/1.3663376

[Large-eddy simulation of a very large wind farm in a stable atmospheric boundary layer](#)

Phys. Fluids **23**, 065101 (2011); 10.1063/1.3589857

[Large eddy simulation study of fully developed wind-turbine array boundary layers](#)

Phys. Fluids **22**, 015110 (2010); 10.1063/1.3291077



Launching in 2016!

The future of applied photonics research is here

OPEN
ACCESS

AIP | APL
Photonics

Large eddy simulation of a large wind-turbine array in a conventionally neutral atmospheric boundary layer

Dries Allaerts^{a)} and Johan Meyers^{b)}

Department of Mechanical Engineering, KU Leuven, Celestijnenlaan 300-Bus 2421, B3001 Leuven, Belgium

(Received 23 October 2014; accepted 23 May 2015; published online 10 June 2015)

Under conventionally neutral conditions, the boundary layer is frequently capped by an inversion layer, which counteracts vertical entrainment of kinetic energy. Very large wind farms are known to depend on vertical entrainment to transport energy from above the farm towards the turbines. In this study, large eddy simulations of an infinite wind-turbine array in a conventionally neutral atmospheric boundary layer are performed. By carefully selecting the initial potential-temperature profile, the influence of the height and the strength of a capping inversion on the power output of a wind farm is investigated. Results indicate that both the height and the strength have a significant effect on the boundary layer flow, and that the height of the neutral boundary layer is effectively controlled by the capping inversion. In addition, it is shown that the vertical entrainment rate decreases for increasing inversion strength or height. In our infinite wind-farm simulations, varying the inversion characteristics leads to differences in power extraction on the order of $13\% \pm 0.2\%$ (for increasing the strength from 2.5 to 10 K), and $31\% \pm 0.4\%$ (for increasing the height from 500 to 1500 m). A detailed analysis of the mean kinetic-energy equation is included, showing that the variation in power extraction originates from the work done by the driving pressure gradient related to the boundary layer height and the geostrophic angle, while entrainment of kinetic energy from the free atmosphere does not play a significant role. Also, the effect of inversion strength on power extraction is energetically not related to different amounts of energy entrained, but explained by a difference in boundary layer growth, leading to higher boundary layers for lower inversion strengths. We further present a simple analytical model that allows to obtain wind-farm power output and driving power for the fully developed regime as function of Rossby number and boundary layer height. © 2015 AIP Publishing LLC. [<http://dx.doi.org/10.1063/1.4922339>]

I. INTRODUCTION

As wind energy is becoming increasingly popular as a renewable energy source, power production from atmospheric winds is gradually shifting towards centralized production in large wind farms. However, turbine performance in large wind farms has been observed to be lower compared to stand-alone operation (Frandsen *et al.*¹). Furthermore, thermal stratification considerably affects the turbulent boundary layer flow, and power deficit in large wind farms has been shown to vary with atmospheric stability (Wharton and Lundquist,² Hansen *et al.*³). Calaf *et al.*⁴ were the first to use large eddy simulations (LES) to study the asymptotic limit of “infinite” wind farms in neutral pressure-driven boundary layers. Johnstone and Coleman⁵ used “direct numerical simulations” with an artificially low Reynolds number to study an infinite wind-turbine array, including Coriolis forces due to the planet’s rotation. LES of wind farms taking into account stability effects were performed by Lu and Porté-Agel⁶ for stable and by Abkar and Porté-Agel^{7,8} for conventionally

^{a)}Electronic mail: dries.allaerts@kuleuven.be

^{b)}Electronic mail: johan.meyers@kuleuven.be

neutral conditions. In this study, large eddy simulations are used to model an infinite wind-turbine array under conventionally neutral conditions, with special attention to the impact of a capping inversion.

Atmospheric stability classification is typically based on the Obukhov length L (see, e.g., Hasager *et al.*⁹), and generally distinguishes between neutral, stable, or unstable (convective) cases. During the past 30 yr, a considerable amount of literature has been published on these three stability types. Amongst many others, Andren *et al.*¹⁰ studied a neutrally stratified boundary layer and compared different LES codes, and Hess and Garratt^{11,12} examined several models of various degrees of sophistication to simulate the same atmospheric flow type. On the other hand, LES of the convective boundary layer include studies by, e.g., Mason¹³ and Moeng and Sullivan.¹⁴ Finally, Beare *et al.*¹⁵ compared the results of a large number of numerical codes for the GABLS case, which is now a well established stable boundary layer case.

The problem with the traditional classification of the atmospheric boundary layer (ABL) is that it is only based on the heat flux at the earth's surface through the definition of the Obukhov length L , and that it does not consider other physical parameters which could be important. Indeed, Csanady¹⁶ first reported that the height of the boundary layer is influenced by the stratification of the free atmosphere aloft. Further, Zilitinkevich and Esau¹⁷ argued that the free atmosphere stratification should be included in the classification of stability types, and, for neutral ABLs, they suggest distinguishing between truly neutral and conventionally neutral flows developing against a neutrally or stably stratified fluid, respectively. Although the focus of some early LES studies was on surface buoyancy forcing, capping inversions were used to limit the boundary-layer height.^{14,18–20} More recently, LES studies of the conventionally neutral atmospheric boundary layer (CNBL) were performed by Zilitinkevich and Esau,¹⁷ Esau,²¹ and Taylor.²² Hess²³ analysed atmospheric data spanning a period of more than 85 yr and compared it with various analytical and numerical models for the CNBL. Based on the available data, Hess concluded that the truly neutral ABL is an idealised case that “does not seem to exist in the atmosphere, or is so rare that it has not been well observed.”

The vertical structure of the CNBL is shown schematically in Figure 1 and can be divided into three layers. The upper layer is the stably stratified free atmosphere with a constant potential-temperature gradient, typically ranging between 1 and 10 K/km.²⁴ In this layer, the flow is non-turbulent and the wind speed G is governed by the geostrophic balance between the horizontal pressure gradient and the Coriolis force,^{25,26}

$$\frac{1}{\rho_0} \frac{\partial p_\infty}{\partial x} = f_c G \sin \alpha, \quad \frac{1}{\rho_0} \frac{\partial p_\infty}{\partial y} = -f_c G \cos \alpha, \quad (1)$$

with α the angle between the geostrophic velocity vector and the x -axis, and $f_c = 2\Omega \sin \phi$ the Coriolis parameter (given the earth's rotation Ω and the latitude ϕ). Thus, the direction of the flow in

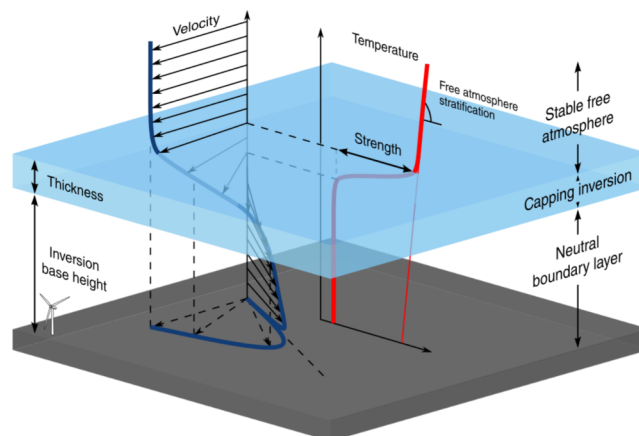


FIG. 1. Three-dimensional schematic view of the conventionally neutral atmospheric boundary layer, showing profiles of the potential temperature and the velocity vector as a function of height.

this upper layer is perpendicular to the pressure gradient. The lowest layer in Figure 1 is the neutral turbulent boundary layer, characterized by a constant potential temperature and a zero surface heat flux. The wind direction here is a result of the force balance between the pressure gradient, the Coriolis force, and the turbulent stress. As a result, the wind inside the boundary layer rotates away from the geostrophic wind direction towards the pressure gradient.

The thin third layer between the upper and lower layers (cf. Figure 1) is called the capping inversion or inversion layer, and most studies of the CNBL do not pay any particular attention to this region. However, the capping inversion often plays an important role in the CNBL due to its strong stability, i.e., the capping inversion can act as a rigid lid on the boundary layer by decelerating any turbulent gusts that try to penetrate into the free atmosphere. Critical parameters that determine the influence of the capping inversion are the height of the inversion base and the temperature jump across the inversion (the inversion strength). For instance, the effect of the capping inversion is negligible when it is situated above the equilibrium height of the truly neutral Ekman boundary layer. This idea was translated by Arya^{27,28} into the similarity parameter $h_* = |f_c| h / u_*$, which relates the actual height of the ABL with the Rossby-Montgomery scale $u_* / |f_c|$, and was later confirmed by Hess,²³ who found that the capping inversion becomes insignificant for $h_* > 0.15$. The importance of the inversion strength for lower inversion heights was first predicted by Lilly,²⁹ stating that the rate of rise of the inversion base is inversely proportional to the inversion strength. Furthermore, Csanady¹⁶ predicted the existence of “an asymptotic depth h , at which no further entrainment takes place,” and this height is determined by the strength of the capping inversion. He proposed an empirical formula that estimates this height as

$$h = A \frac{\theta_0}{g \Delta \theta} u_*^2, \quad (2)$$

with $A \approx 500$ an empirical parameter. This estimation was later confirmed by Tjernström and Smedman³⁰ using airborne measurement data over the Baltic Sea.

Despite the strong indications in the studies mentioned here, many formulations of the boundary-layer height only use the free-atmosphere Brunt-Väisälä frequency N as scaling parameter^{31,32} and completely ignore the effects of capping inversions. Moreover, all aforementioned LES studies of the CNBL describe the neutral boundary layer under varying free atmosphere stratification but do not consider different inversion heights or strengths. However, based on zero-order model analysis of the entrainment in a CNBL, Tennekes³³ concluded that the potential-temperature gradient above the ABL plays no role when the initial inversion height or strength is very high. Similarly, when discussing the inversion strength, Hess²³ mentioned that “the value of this jump may be more important than the precise value of N .”

The aim of the current study is to assess the performance of large wind farms in the presence of capping inversions with varying characteristics. In large wind farms, the energy extraction by the turbines is dominated by downward turbulent transport of kinetic energy from the airflow above the farm.⁴ Moreover, wind farms enhance vertical entrainment of air into the farm and increase the boundary-layer growth above the farm. The capping inversion has exactly the opposite effect, i.e., the turbulent entrainment process is slowed down and further deepening of the boundary layer is prevented. Hence, it is to be expected that the inversion layer will have an influence on the amount of energy that can be transported towards the turbines.

In this paper, we will focus on offshore wind farms, where CNBLs occur more often compared to onshore, since the surface heat flux tends to be smaller at sea.³⁴ Furthermore, low inversion base heights are much more probable over sea. For example, Brost *et al.*³⁵ reported inversion heights as low as 400 m for the marine stratocumulus experiment, and similar heights were observed in several other measurement campaigns.^{30,36,37} Such low inversion layers will have stronger effects on wind-farm performance than higher land-based inversions. The temperature profiles reported by Grant³⁷ and Brost *et al.*³⁵ for the KONTUR and marine stratocumulus experiments are representative for offshore CNBLs, and Hess²³ estimated the inversion strength and thickness for these experiments to range between 2.7–8.7 K and 50–175 m, respectively.

The paper has been organised in the following way. In Sec. II, the simulation code is explained and the various LES cases are described. Next, an overview of the CNBL structure and its general characteristics are given in Sec. III. The influence of the capping-inversion parameters on the boundary layer and the wind-farm performance is discussed in Sec. IV. Subsequently, the observed differences are analysed by means of a closed analytical model, which is developed in Sec. V. Conclusions are summarized in Sec. VI.

II. LES METHODOLOGY AND NUMERICAL SETUP

A. Governing equations and LES code

The governing equations for LES are filtered versions of the continuity, momentum, and potential-temperature equations,^{26,38}

$$\frac{\partial \tilde{u}_i}{\partial x_i} = 0, \quad (3)$$

$$\frac{\partial \tilde{u}_i}{\partial t} + \tilde{u}_j \frac{\partial \tilde{u}_i}{\partial x_j} = -\frac{\partial \tilde{p}^*}{\partial x_i} + \delta_{i3} g \frac{\tilde{\theta} - \theta_0}{\theta_0} + f_c \epsilon_{ij3} \tilde{u}_j - \frac{\partial \tau_{ij}^r}{\partial x_j} + f_i - \frac{1}{\rho_0} \frac{\partial p_\infty}{\partial x_i}, \quad (4)$$

$$\frac{\partial \tilde{\theta}}{\partial t} + \tilde{u}_j \frac{\partial \tilde{\theta}}{\partial x_j} = -\frac{\partial q_j^{sgs}}{\partial x_j}. \quad (5)$$

The index i equals 1, 2, 3 and corresponds to the streamwise (x,u), spanwise (y,v), and vertical (z,w) direction and component, respectively. Further, \tilde{u}_i are the components of the three dimensional filtered velocity field and $\tilde{\theta}$ is the three dimensional filtered potential-temperature field. In Eq. (4), the Boussinesq approximation has been applied to obtain the buoyancy term, in which g represents the gravitational acceleration, and θ_0 is the background adiabatic base state. The filtered pressure \tilde{p} is split up in a linear varying mean background pressure p_∞ , and a fluctuating part \tilde{p}^* . The mean horizontal pressure gradient ∇p_∞ is related to the geostrophic wind speed G by geostrophic balance (1) above the boundary layer. Furthermore, $\tau_{ij}^{sgs} = \tau_{ij}^r + \delta_{ij} \tau_{kk}/3$ are the subgrid-scale stresses, and q_j^{sgs} is the subgrid-scale heat flux. Only the traceless part of the subgrid stress tensor is modelled (cf. further below); the trace is absorbed into the pressure, leading to a modified pressure $\tilde{p}^* = \tilde{p}/\rho_0 + \tau_{kk}/3$. Finally, the Coriolis force is included using the Coriolis parameter $f_c = 2\Omega \sin \phi$, and the forces f_i represent the effect of the wind turbines on the flow (see further below).

For the conventionally neutral boundary layer, the top boundary conditions are a zero stress condition for the horizontal velocity, a zero vertical velocity, and a fixed potential temperature, assuming that the domain is sufficiently high, so that the temperature at the top is not influenced by the boundary layer. For the lower boundary condition, we employ a classic wall stress formulation based on the Monin-Obukhov similarity theory for neutral boundary layers,³⁸

$$\tau_{w1} = -\left(\frac{\kappa}{\ln z/z_0}\right)^2 \left(\hat{u}^2 + \hat{v}^2\right)^{0.5} \hat{u}, \quad (6)$$

$$\tau_{w2} = -\left(\frac{\kappa}{\ln z/z_0}\right)^2 \left(\hat{u}^2 + \hat{v}^2\right)^{0.5} \hat{v}, \quad (7)$$

with κ the von Kármán constant and z_0 a surface roughness length. Locally averaged horizontal velocities, denoted with a hat, are used to match the average wall stress with the classic log law.³⁹ No stability correction functions are needed in the wall model because the surface heat flux is set to zero.

The deviatoric part of the subgrid-scale stress τ_{ij}^r and the subgrid-scale heat flux q_j^{sgs} is parametrized by a mixing length model,

$$\tau_{ij}^r = -2K_m S_{ij}, \quad q_j^{sgs} = -K_h \frac{\partial \tilde{\theta}}{\partial x_j}, \quad (8)$$

with the filtered rate of strain $S_{ij} = 0.5 (\partial \tilde{u}_i / \partial x_j + \partial \tilde{u}_j / \partial x_i)$. Following the \mathcal{S}_σ model proposed by Stevens *et al.*,⁴⁰ the eddy coefficients K_m and K_h are expressed as

$$K_m = (c_s l)^2 S \sqrt{1 - \frac{c_h}{c_m} Ri}, \quad K_h = \frac{c_h}{c_m} K_m, \quad (9)$$

with the characteristic filtered rate of strain $S = (2S_{ij}S_{ij})^{0.5}$, the Richardson number $Ri = N^2/S^2$, and the Brunt-Väisälä frequency $N = [(g/\theta_0) \partial \tilde{\theta} / \partial z]^{1/2}$. Stevens *et al.*⁴⁰ define the characteristic length-scale l as the minimum of the grid size Δ and the stability related length-scale $l_s = c_l \sqrt{e} N^{-1}$. In the current study, we replace the minimum function by the smoother geometric mean function and include a classic wall damping of the length-scale near the bottom surface.⁴¹ Thus, we arrive at a length-scale that is given by

$$l^{-n} = \Delta^{-n} + l_s^{-n} + [\kappa(z + z_0)]^{-n}, \quad (10)$$

where we take $n = 2$.

The forces exerted by the wind turbines on the flow are computed with an actuator disk model (ADM). This method represents the wind turbines as porous disks and has been used in many earlier LES studies.^{4,42–45} In the current work, we apply a non-rotating actuator disk method in which tangential forces are neglected. Wu and Porté-Agel⁴⁶ demonstrated that the non-rotating ADM allows an adequate representation of the overall wake structure behind the turbines except in the very near wake ($x/D < 3$). As the focus of the study lies on the interaction between the ABL and the wind farm as a whole, non-rotating ADM is found to be sufficiently accurate. The implementation corresponds to the version used in Refs. 4, 44, and 45. The total thrust force exerted by a turbine on the flow is

$$F_t = -\rho_0 \frac{1}{2} C'_T \langle \tilde{u}^T \rangle_d^2 \frac{\pi}{4} D^2, \quad (11)$$

with $\langle \tilde{u}^T \rangle_d$ the disk-averaged and time-filtered velocity.⁴⁴ In the current study, a one-sided exponential time filter with a time constant of 1 min is used. The disk-based coefficient C'_T represents the overall effect of blade lift and drag forces on the air flow at the rotor disk,^{4,44} nondimensionalized with the axial velocity at the rotor disk instead of an upstream undisturbed reference velocity. The thrust force is first distributed constant over the disk area in a coordinate system in the turbine rotor plane. Subsequently, the wind-turbine forces f_i are obtained by filtering the distributed thrust force onto the LES grid by means of a Gaussian convolution filter. Details can be found in Refs. 4 and 44.

B. Wind angle controller

As shown in Figure 1, the addition of Coriolis forces in the momentum equation causes the wind direction in the boundary layer to change with height. As a result, the effective wind direction at the hub height is not known *a priori*, i.e., it depends on the turbulent dissipation and the wind-farm power production. In order to ensure the same geometrical pattern of wind turbines in all simulations, the wind speed at hub height should always be directed in the same way. This is achieved by regulating the direction of the driving pressure gradient through a wind angle controller. Similar to the action of the flow-direction controller in the study of Sescu and Meneveau,⁴⁷ pseudo-forces induced by a rotation of the reference frame are added to the momentum equation. The rotation speed is chosen equal to the rotation of the wind velocity at hub height, thereby cancelling out any change in the average wind direction,

$$\omega = \frac{\phi_h^n - \phi_h^{n-1}}{\Delta t}, \quad \tan \phi_h = \frac{\langle V(z_h) \rangle}{\langle U(z_h) \rangle}, \quad (12)$$

with ϕ_h^n the average wind direction at hub height at time step n . A first-order time filter with time constant σ is applied to average out rapid turbulent fluctuations. Further, a term proportional to the misalignment of the wind velocity vector is added to prevent steady state errors. The effective rotation speed of the reference frame is then given by

$$\omega_e = \bar{\omega} + \beta(\phi_h - \phi_{h,\text{ref}}). \quad (13)$$

The tuning parameters of the wind angle controller are set to $\sigma = 3.33$ min and $\beta = 2$ hr⁻¹. As the controller induces pseudo-forces, this could be interpreted as a change to the Coriolis parameter f_c . However, the effective rotation speed is at least two orders of magnitude smaller than the Coriolis parameter at all times, so the influence of this rotation on the shear stress profiles and the atmospheric boundary layer height is negligible.

C. CNBL cases and numerical setup

The in-house LES code SP-Wind is used, which is an updated version of the KU Leuven code, e.g., used by Calaf *et al.*,⁴ that includes effects of thermal stratification. In horizontal directions, pseudo-spectral discretization and periodic boundary conditions are used,⁴⁸ whereas the vertical direction is discretized with a fourth-order energy-conservative finite difference scheme.⁴⁹ Time advancement is based on a classic four-stage fourth-order Runge-Kutta scheme, and the time step is computed with a Courant-Friedrichs-Lewy number equal to 0.4. The influence of the capping inversion on large wind farms is investigated based on a suite of LES simulations with different inversion properties. Table I gives an overview of the parameters that vary amongst the different simulations as further explained below.

For typical offshore values of friction velocity $u_* = 0.28$ m/s and capping-inversion strength $\Delta\theta = 2.5$ K (cf. Ref. 35), and using Eq. (2), the equilibrium height is estimated to be about 450 m. Therefore, we choose a base height of 500 m and strength of 2.5 K for the baseline case REF. The other cases explore the effect of inversion strength and height, covering a range of 0–10 K, and 200–1500 m, respectively (see Table I). Note that, e.g., a height of 1500 m would be quite uncommon for offshore boundary layers, but is included for sake of evaluating the parameters over a wide range. Cases S00 and H02 are chosen such that the initial inversion base height is below the equilibrium height, so that also non-equilibrium CNBLs are studied. The domain size amounts to 6 km and 3 km in streamwise and spanwise directions, and the height of the domain is set to 1 km in most cases. Cases S00, H10, and H15 are simulated in a higher domain in order to cope with large initial heights or strong boundary-layer growth.

Several studies have revealed that resolution of the buoyancy scale $L_b = 2\pi u_{rms}/N$ is necessary to capture the stratified turbulent energy cascade.^{50–52} As a result, simulation of the strongly stable inversion layer is a challenging numerical task that requires very fine vertical grid sizes. Khani and Waite⁵³ found a critical grid spacing of $\Delta < 0.17L_b$ for LES with a standard Smagorinsky model. In the current study, grid sizes are varied amongst the LES simulations to guarantee a grid resolution of $37.5 \text{ m} \times 9.375 \text{ m} \times 3.9 \text{ m}$ in all simulations. With a minimum buoyancy scale in all simulations above 30 m, the vertical grid resolution is sufficient to model the inversion layer with reasonable accuracy.

Atmospheric conditions are chosen to represent a conventionally neutral atmospheric boundary layer over sea. The drag due to ocean waves is simply modelled by a surface roughness length z_0 , which is set to a representative value of⁵⁴ 2×10^{-4} m. Similar values can be found in the literature, e.g., Hess²³ uses 8×10^{-5} and 3×10^{-4} m to represent the sea surface. The potential temperature of the neutral boundary layer θ_m is 15 °C and the free atmosphere stratification γ is 1 K/km for all

TABLE I. Overview of the varying parameters of the suite of LES cases.

	$h_{0(\text{init})}$ (m)	$\Delta\theta_{(\text{init})}$ (K)	$L_x \times L_y \times L_z$ (km × km × km)	$N_x \times N_y \times N_z$
REF	500	2.5	$6 \times 3 \times 1$	$160 \times 320 \times 256$
S00	500	0	$6 \times 3 \times 1.75$	$160 \times 320 \times 448$
S10	500	10	$6 \times 3 \times 1$	$160 \times 320 \times 256$
H02	200	2.5	$6 \times 3 \times 1$	$160 \times 320 \times 256$
H10	1000	2.5	$6 \times 3 \times 1.75$	$160 \times 320 \times 448$
H15	1500	2.5	$6 \times 3 \times 2.5$	$160 \times 320 \times 640$

cases. The reference temperature θ_0 is taken to be equal to θ_m . Further, the atmosphere is assumed to be barotropic with a geostrophic wind speed $G = 10$ m/s. The surface Rossby number $Ro = G/z_0 f_c$ is equal to 5×10^8 , corresponding to a latitude of $\phi = 43.43^\circ$.

The wind farm under consideration consists of 48 turbines, characterized by a hub height $z_h = 100$ m and a diameter $D = 100$ m. The turbine grid comprises eight rows (at a distance $s_x \times D$) containing six turbines (at a distance $s_y \times D$), with $s_x = 7.5$ and $s_y = 5$. All simulations use $C'_T = 4/3$, similar to Calaf *et al.*⁴

In the absence of subsidence and heat radiation, the potential-temperature distribution in a CNBL is critically dependent on the heating history.³³ Consequently, the choice of initial condition for the potential temperature has a direct impact on the outcome of a simulation. The typical linear potential-temperature profile used in most LES studies does not allow any control over the inversion height nor strength. Instead, we initialize the potential-temperature profile using the smooth curve proposed by Rampanelli and Zardi,⁵⁵

$$\theta(z) = \theta_m + a \frac{\tanh(\eta) + 1}{2} + b \frac{\ln[2 \cosh(\eta)] + \eta}{2}, \quad (14)$$

where η is a dimensionless height and a and b are tuning parameters directly related to inversion parameters such as the strength $\Delta\theta$, the thickness Δh , and the height of the inversion base h_0 , center h_1 , and top h_2 (see Figure 2). The initial inversion thickness is set to $\Delta h_{(\text{init})} = 100$ m in all simulations; other parameters are given in Table I and are related to a varying strength or base height of the inversion layer.

Next to the potential-temperature profile, also the velocity needs to be carefully initialized. Below the capping inversion, the velocity profile is initialized with a similarity profile for neutral boundary layers⁵⁶ such that the transition time towards a conventionally neutral velocity profile is minimal. We use

$$u_{\downarrow}(z) = \frac{u_*}{\kappa} \left[\ln \frac{z}{z_0} + f_u(\zeta) \right], \quad (15)$$

$$v_{\downarrow}(z) = -\frac{u_*}{\kappa} f_v(\zeta) \text{sign} f, \quad (16)$$

where $f_u = 1.57\zeta - 2.68\zeta^2$ and $f_v = 13.2\zeta - 8.70\zeta^2$ are functions of the non-dimensional height $\zeta = z/h_0$, and u_* is the friction velocity. In the free atmosphere, the horizontal momentum equations describe an undamped harmonic oscillator.⁵⁷ Therefore, the velocity profiles u_{\uparrow} and v_{\uparrow} above the capping inversion are initialized with the prescribed geostrophic wind velocity, so that large undamped inertial oscillations are avoided. The free-atmosphere profile is merged with the neutral

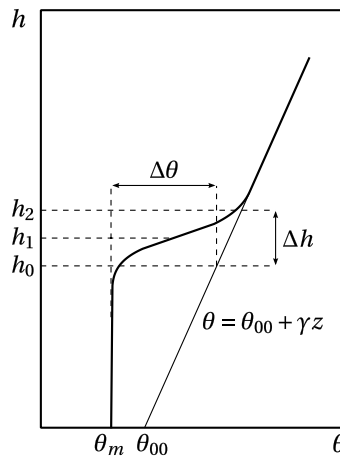


FIG. 2. Smooth curve used as initial potential-temperature profile. Characteristic parameters defining the capping inversion are indicated. Reprinted with permission from G. Rampanelli and D. Zardi, “A method to determine the capping inversion of the convective boundary layer,” *J. Appl. Meteorol.* **43**(6), 925–933 (2004). Copyright 2004 American Meteorological Society.

boundary-layer profile well below the region of the inversion layer using a tanh function,

$$u = u_{\downarrow}(z) \frac{1 - \tanh[(\zeta - 0.5)2h_0/\delta]}{2} + G \cos \alpha \frac{1 + \tanh[(\zeta - 0.5)2h_0/\delta]}{2}, \quad (17)$$

and similar for v . Thus, both layers are smoothly merged around $z = h_0/2$ in a merging region with width $\delta = 100$ m.

In order to trigger turbulence in the simulations, random divergence-free perturbations are added to the velocity profile. These perturbations have an amplitude of $0.1G$ and are added below 100 m only. In this way, the initial “non-physical” random noise is not directly interacting with the inversion layer. As we are interested in the development of a wind-turbine array boundary layer from realistic initial atmospheric conditions, the simulations first aim at reaching a stationary or quasi-stationary state under conventionally neutral conditions. According to Zilitinkevich *et al.*,³² equilibration is typically reached after 16–24 model hours. Thus, the initial condition is progressed in time for 20 h before the wind farm is inserted. During this time, the initial random noise evolves into turbulence and fills up the boundary layer under the capping inversion. After these initial 20 h, the wind turbines are switched on (cf. further discussion Sec. III).

III. GENERAL CHARACTERISTICS OF THE CNBL WITH WIND TURBINES

In this section, the characteristics of the CNBL with an immersed wind farm will be discussed based on the LES results of the baseline case. First, in Sec. III A, the growth of the CNBL in time is discussed. Subsequently, velocity profiles and geostrophic angle are discussed in Sec. III B, and stress profiles are presented in Sec. III C.

A. Boundary-layer growth

First of all, we discuss the behaviour of the CNBL height in function of time both during the 20-h initialization and the subsequent wind-farm simulation. In the literature, several methods are proposed to estimate the height of the boundary layer; three of them are used in the current study. A first estimate is based on the height where the turbulent shear stress vanishes, following Kosović and Curry.⁵⁸ They use the height where the turbulent stress equals 5% of the wall stress (u_*^2) and linearly extrapolate this height to obtain the height for which the stress vanishes. We determine the height h_M based on this procedure, but in the presence of wind farms, we use 5% of the sum of wall stress and surface-averaged wind-turbine thrust forces (u_{*hi}^2 , with u_{*hi} the friction velocity above the wind farm—cf. Eq. (18) for further details). Johnstone and Coleman⁵ suggest an alternative estimate h_G for the boundary-layer height, defined as the height where the mean horizontal velocity lines up with the geostrophic wind for the first time. A third estimate for the boundary-layer height originates from analytical models used for entrainment parametrization in convective boundary layers, the so-called zero- and first-order jump models.^{29,33,59,60} In these simplified models, the vertical heat flux is assumed to attain its minimum at the inversion base. As discussed further below, the heat flux in the CNBL shows similar behaviour, so the height h_T where the vertical heat flux attains its minimum serves as a third estimate for the boundary-layer height.

Figure 3 compares the three estimates of the boundary-layer height h_M , h_G , and h_T with the base h_0 , center h_1 , and top h_2 of the inversion layer as a function of time. The inversion characteristics h_0 , h_1 , and h_2 at every time step are determined through a best-fit analysis of the instantaneous vertical potential-temperature profile with the smooth test function in Eq. (14).

As discussed in Sec. II C, simulations are started from random noise and run without wind farm for 20 h before the turbines are switched on. In Figure 3, this development phase is clearly visible. In particular, we observe that all measures for boundary-layer height start at an artificially low value, related to the fact that random noise is only added in the first 100 m of the domain. Subsequently, the boundary-layer estimates h_M and h_T indicate that the turbulent shear stress and

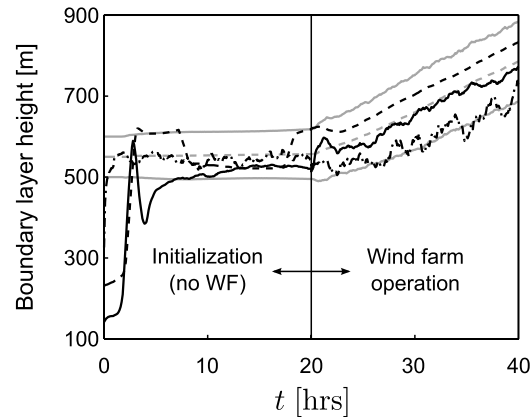


FIG. 3. Time evolution of boundary-layer height estimators h_M (solid black line), h_G (dashed black line), and h_T (dashed-dotted black line) and of the vertical structure of the capping inversion, including height of the base h_0 (lower solid grey line), center h_1 (dashed grey line), and top of the layer h_2 (upper solid grey line), for the baseline simulation REF.

the turbulent heat flux grow rapidly towards the inversion layer. After approximately 2.5 h, the different measures for boundary-layer height reach the inversion layer. During the remaining time, the boundary layer slowly evolves towards an equilibrium state. Near the end of the initialization period, the boundary-layer growth attains a small constant value (less than 0.5 m/h) indicative of quasi-stationary behaviour. Moreover, we observed that the relative difference between the hourly averaged velocity and shear stress profiles is less than one and three percent, respectively (not shown here). It is thus reasonable to assume that the flow has reached quasi-stationary conditions, and the development of the wind-turbine array boundary layer can be studied starting from this boundary layer state.

When the wind turbines are switched on, an additional transient occurs. After approximately 10 h of wind farm operation, the boundary layer stabilizes again into a regime of small, but constant growth. The effective growth rate in the last 10 h of the simulation is small (about 12 m/h). Therefore, to discuss and compare averaged flow profiles, we will look at averages of the CNBL over the last 10 h.

Examining the estimators in more detail during wind-farm operation, we observe in Figure 3 that h_M corresponds reasonably well with the center of the inversion layer h_1 , whereas h_G generally lies between h_1 and h_2 . The estimation based on the turbulent heat flux h_T shows good agreement with the inversion base height. Based on these observations, we will use h_1 to estimate the top of the CNBL with wind turbines in the remainder of this study.

Finally, a sample of instantaneous velocity profiles after 35 h of simulation is shown in Figure 4. The black lines in 4(a) and 4(b) mark the locations of the wind-turbine disks. In Figure 4(a), the x-y plane is taken at $z = 100$ m and cuts through the wind-turbine centers, clearly showing the velocity deficit in the wakes behind the turbines. Further, elongated high-speed streaks are visible along the mean flow direction. Figure 4(b) shows an x-z cut through the middle of a column of wind turbines. Here, strong ejection and sweep motions are observed up to approximately 750 m. At higher altitudes, no turbulent fluctuations occur: this is caused by the presence of the capping inversion, which confines turbulent gusts to the boundary layer.

B. Mean velocity profiles and geostrophic angle

Profiles of mean velocity magnitude at different simulation times are presented in Figure 5(a). In the literature, it has been shown that the velocity profile in fully developed wind-farm boundary layers (with wind turbines situated within the inner layer) is expected to show a double log layer.^{4,61} In Figure 5(a), it is clear that, at the start of the wind-farm operation, the velocity profiles quickly transform from the simple log layer in the absence of wind turbines (see the dashed line in

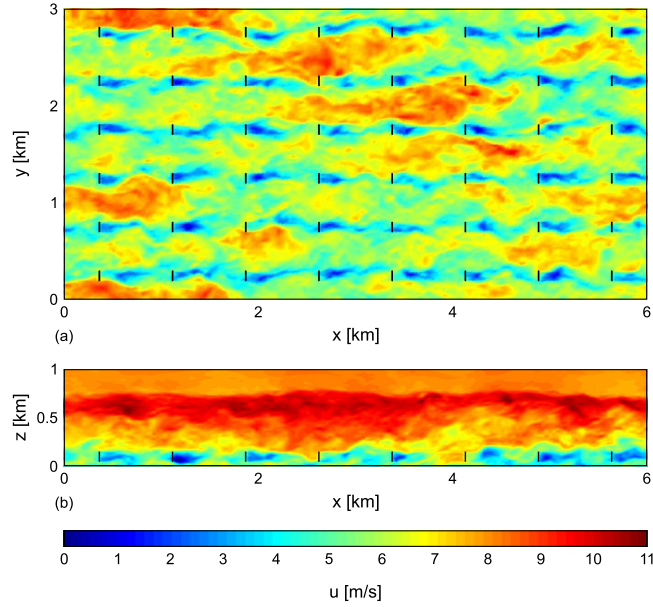


FIG. 4. Instantaneous contours of streamwise velocity from LES for baseline case REF. (a) An $x-y$ plane at $z = 100$ m through the wind-turbine centers (the location of the wind-turbine disks is shown with vertical black lines). (b) An $x-z$ plane cutting through the middle of a column of wind turbines.

Figure 5(a)) into a double log layer. Below the turbine region, a clear logarithmic region with surface roughness length $z_{0,lo} = 2 \cdot 10^{-4}$ m and characteristic friction velocity $u_{*lo} = (\tau_w)^{1/2}$ equal to 0.21 m/s can be observed. Above the farm, a second log layer characterized by a friction velocity u_{*hi} is found. Due to the low inversion layer, this second log layer only extends up to about 500 m. Higher up, outer-layer effects start to influence the velocity profile.

The friction velocity u_{*hi} corresponds to the total friction of the surface and the wind turbines.^{4,61} In the presence of Coriolis forces, it corresponds to

$$u_{*hi}^2 = \|\tau_w + f_t\| \approx \|\tau_w\| + \|f_t\|, \quad (18)$$

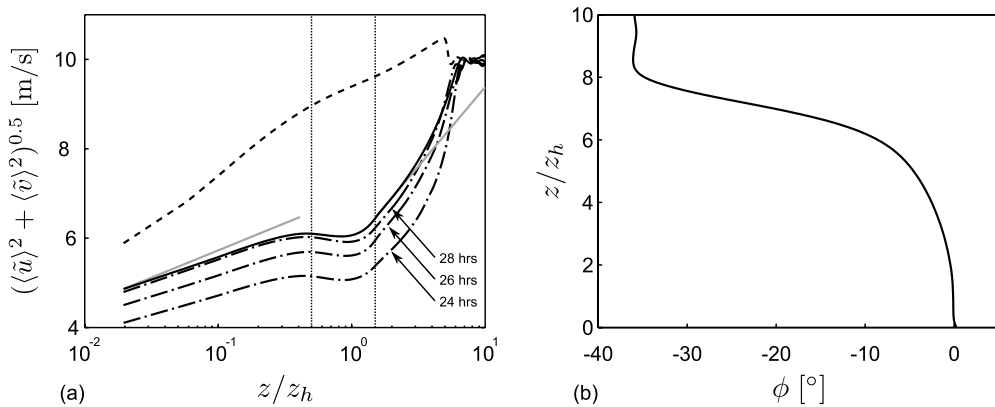


FIG. 5. Horizontally averaged profiles of mean velocity magnitude and direction for the baseline case REF. (a) Profiles of mean velocity magnitude after the start-up phase of 20 h (dashed line), at intermediate times (dashed-dotted lines), and averaged over the last 10 h of wind-farm operation (solid line). Vertical dotted lines mark the bottom and top of the turbine region, and reference lines for the log-layers are shown in grey. (b) Mean wind direction, averaged over the last 10 h of wind-farm operation.

with τ_w the wall stress and $\mathbf{f}_t = \mathbf{F}_t / (s_x s_y D^2)$ the area-averaged thrust force of the wind farm, which is by definition directed along the x -axis. Although τ_w and \mathbf{f}_t need not be perfectly aligned in the presence of Coriolis forces, the angle between these forces turns out to be a few degrees only, so that the vectorial sum may be approximated by the sum of force magnitudes. Using Eq. (18), the friction velocity u_{*hi} for the baseline case is found to be 0.62 m/s. Finally, matching the velocity profile above the turbine region with a log law based on u_{*hi} yields $z_{0,hi} = 2.26$ m.

The vertical profile of average flow angle is shown in Figure 5(b). Due to the wind-angle controller, the wind speed at hub height is directed along the x -axis. The geostrophic angle α is defined as the change in wind direction between the geostrophic wind vector in the free atmosphere and the x -axis, which corresponds to the direction of the wind flow at hub height. The CNBL with wind turbines and a low capping inversion appears to be characterized by a large geostrophic angle. As seen in Figure 5(b), the geostrophic angle for the baseline case is about -36° . By comparison, Johnstone and Coleman⁵ report a geostrophic angle of -32.8° for a turbulent Ekman boundary layer without capping inversion, but with a more densely spaced wind farm ($s_x = s_y = 5D$) and a disk-based thrust coefficient equal to the Betz limit, i.e., $C_T = 2$. We further observe that more than 75% of the change in wind direction occurs inside the thin inversion layer. The occurrence of such a directional jump at the inversion layer was also reported by Brost *et al.*,³⁵ for small inversion heights in marine stratocumulus layers.

C. Stress and heat-flux profiles

We now look at the shear stress profiles in the CNBL. The components of the total shear stress are defined as the sum of the Reynolds, dispersive, and mean SGS stress components,^{4,62}

$$\tau_{xz}(z) = -\langle \tilde{u}'\tilde{w}' \rangle(z) - \langle \tilde{u}''\tilde{w}'' \rangle(z) - \langle \tau_{xz}^r \rangle(z), \quad (19)$$

$$\tau_{yz}(z) = -\langle \tilde{v}'\tilde{w}' \rangle(z) - \langle \tilde{v}''\tilde{w}'' \rangle(z) - \langle \tau_{yz}^r \rangle(z), \quad (20)$$

using a bar for time averaging and brackets for horizontal averaging. Further, $\tilde{u}'_i = \tilde{u}_i - \tilde{\bar{u}}_i$ and $\tilde{u}''_i = \tilde{u}_i - \langle \tilde{\bar{u}}_i \rangle$. The dispersive stress components $\langle \tilde{u}''\tilde{w}'' \rangle$ and $\langle \tilde{v}''\tilde{w}'' \rangle$ arise due to correlations among the spatially non-homogeneous mean horizontal and mean vertical velocities.⁶³

The different components of the various shear stresses are shown in Figure 6(a). We observe that the momentum transport in the CNBL with wind turbines is mainly provided by the Reynolds stresses. The streamwise dispersive stresses are only important inside the turbine region, and

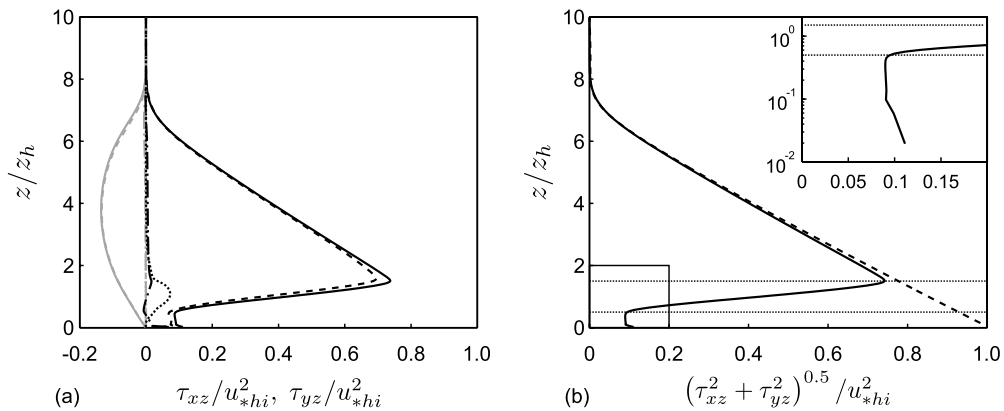


FIG. 6. Vertical profiles of shear stresses, averaged over horizontal planes and over the last 10 h of wind-farm operation, for the baseline case. (a) Streamwise (black lines) and spanwise (grey lines) shear stress components, including total shear stresses (solid lines), Reynolds stresses (dashed lines), subgrid-scale stresses (dashed-dotted lines), and dispersive stresses (dotted lines). (b) Total shear stress magnitude (solid line) and expected stress profile using rhs of Eqs. (21) and (22) (dashed line). In the top right corner, the lowest 20% of the domain is magnified and plotted in semi-logarithmic scale. The horizontal dotted lines mark the bottom and top of the turbine region.

only about 11% of the Reynolds stresses. The spanwise dispersive stresses are completely negligible. Furthermore, the mean subgrid-scale stresses are only significant close to the ground in the x -direction. In the y -direction, mean subgrid-scale stresses remain small throughout the boundary layer, as at the ground the total spanwise shear stress is nearly zero. Finally, above the inversion layer, all shear stress components are zero. In this region, only Coriolis forces and pressure gradient contribute to the force balance.

The magnitude of the total shear stress is shown in Figure 6(b). In the atmospheric boundary layer community, the concept of a constant stress layer is widely used, in which it is assumed that the stress varies less than 10% in the inner layer of the ABL ($z/h_1 \ll 1$). Below the turbine region, we can indeed observe a constant stress layer in which $\|\boldsymbol{\tau}\| \approx u_{*lo}^2$ within 20% accuracy (see top right corner in Figure 6(b)), as, e.g., also observed in Calaf *et al.*⁴ Above the turbine region, the assumption of a constant stress layer no longer holds as the turbines reach up to about 20% of the shallow boundary layer height. Here, the expected shear stress profile follows from integrating the time and horizontally averaged momentum equations, i.e.,

$$\tau_{xz}^e(z) = \int_z^H f_c (\langle \bar{u}_2 \rangle(z') - G \sin \alpha) dz', \quad (21)$$

$$\tau_{yz}^e(z) = \int_z^H f_c (-\langle \bar{u}_1 \rangle(z') + G \cos \alpha) dz'. \quad (22)$$

In Figure 6(b), the magnitude of the total shear stress is close to linear near the top of the wind-turbine region and reaches a maximum value of about $0.75u_{*hi}^2$. Note that the friction velocity of the second log layer is defined as the sum of the wall stress and the area-averaged thrust force (see Eq. (18)), and that it can be found to be extrapolating the expected shear stress to the ground, i.e., $u_{*hi}^2 \approx \tau(z)/(1 - z/h_1)$. The linear behaviour extends up to about 500 m, i.e., up to the same height as the second log layer in Figure 5(a).

Based on this observation, we can define an open channel flow that approximates the CNBL in its lower part. The height of this equivalent channel flow h_{eq} is found by linearly extrapolating the lower part of the CNBL shear stresses. This yields a height of 686 m, which is somewhere halfway between the bottom and center of the inversion layer. The corresponding pressure gradient is equal to $\rho_0 u_{*hi}^2 / h_{eq}$. We find that it is about 6% lower than the streamwise CNBL pressure gradient $\partial p_\infty / \partial x$ for the baseline case (remember that in the CNBL, the Coriolis forces are added in the force balance).

Finally, we look at potential-temperature and heat-flux profiles in Figure 7. From the horizontally averaged profiles at various simulation times in Figure 7(a), it is clear that the mean

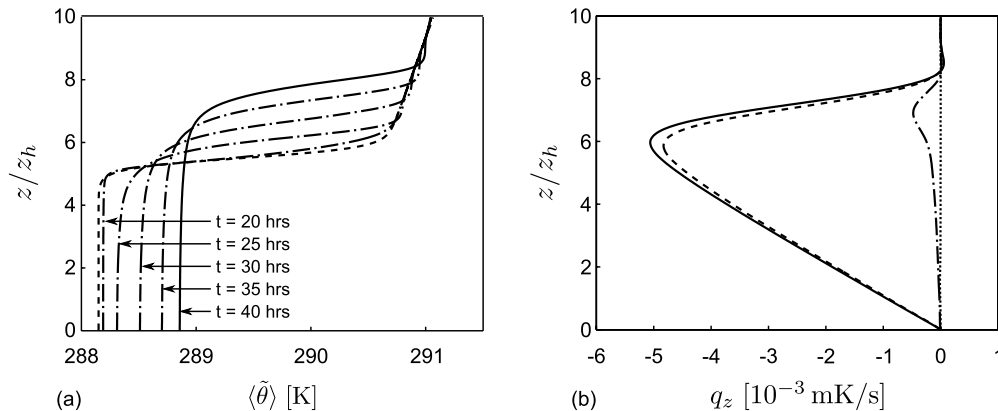


FIG. 7. Horizontally averaged profiles of potential temperature and heat flux for the baseline case. (a) Profiles of mean potential temperature, including the initial potential-temperature condition (dashed line), several profiles at intermediate times (dashed-dotted lines), and the potential-temperature profile after 20 h of wind-farm operation (solid line). (b) Heat fluxes, averaged over the last 10 h of wind-farm operation, including total heat flux (solid lines), turbulent heat flux (dashed lines), subgrid-scale heat flux (dashed-dotted lines), and dispersive heat flux (dotted lines).

potential temperature hardly changes during initial start-up phase of 20 h. After switching on the wind turbines, the potential temperature evolves with a nearly constant speed, and an increase in both the BL height as well as the mixed-layer temperature is observed. Throughout the whole simulation, however, the shape of the profile remains very similar. Note that this allows us to effectively use the fit of Rampanelli and Zardi for the estimation of capping-inversion strength and height.

The total vertical heat flux q_z and its components are defined similar to the total shear stresses,

$$q_z(z) = \langle \tilde{w}'\tilde{\theta}' \rangle(z) + \langle \tilde{w}''\tilde{\theta}'' \rangle(z) + \langle q_z^{sgs} \rangle(z). \quad (23)$$

In Figure 7(b), the total heat flux attains a minimum at the base of the inversion layer. Below the inversion, the heat flux is approximately linear and the boundary layer warms up uniformly with height. Above the inversion, warm air is cooled down due to the entrainment process. In the free atmosphere, the heat flux is zero and the potential temperature stays equal to its initial value. The dispersive heat flux is very small throughout the domain, indicating that the mean vertical velocity and the mean potential temperature are rather uncorrelated. The subgrid-scale fluxes are small everywhere except in the inversion layer, where they attain values up to 10% of the maximum total heat flux (in absolute value). In this highly stable region, turbulent length scales are reduced and a substantial part of the heat transport is not resolved by the LES grid but modelled through the subgrid-scale model.

IV. CNBL AND WIND-FARM BEHAVIOUR UNDER VARYING CAPPING INVERSIONS

In this section, the results of the different LES cases are compared, and the impact of the various inversion-layer characteristics on the CNBL behaviour is assessed.

Figure 8 shows the evolution of the boundary-layer height h_1 and the geostrophic angle α for the different LES cases. In Figure 8(a), all simulations with an initial inversion layer above the equilibrium height (REF, S10, H10, and H15) show almost no growth during the first 20 h (i.e., in the absence of wind turbines). In contrast, simulations S00 and H02 are not in equilibrium and attain a constant growth rate.

Once the wind farm is switched on, the turbines induce extra friction, thereby increasing the equilibrium height of the CNBL. As a result, the boundary layer starts growing in all simulations. Cases REF, S10, H10, and H15 show a modest, nearly constant boundary layer growth rate during the whole wind-farm operation, and the lowest growth rates correspond to the cases with high or strong inversion layers. The increase in boundary-layer height over the 20 h of wind-farm operation ranges between 30 and 230 m (1.5–11.5 m/h). On the other hand, cases S00 and H02 show large growth, as they are farther away from the equilibrium height. Although case S00 started without an

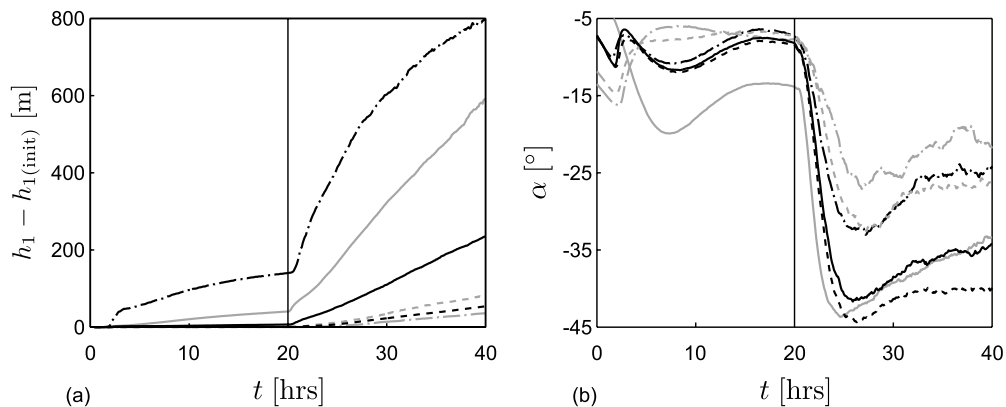


FIG. 8. Boundary-layer growth $h_1 - h_{1(\text{init})}$ (a) and geostrophic angle α (b) as a function of time for the cases REF (solid black line), S10 (dashed black line), S00 (dashed-dotted black line), H02 (solid grey line), H10 (dashed grey line), and H15 (dashed-dotted grey line).

inversion layer, we observe that, near the end of the simulation, a weak inversion layer (about 0.7 K) is formed, causing a slow down of the boundary-layer growth. However, at this time, the boundary layer has grown by more than 800 m.

In Figure 8(b), the evolution of the geostrophic angle is shown. Here, the trends are somewhat different. The geostrophic angle increases with increasing inversion strength, but decreases with increasing inversion heights. For all cases, the geostrophic angle increases significantly in magnitude during the first 5 h of wind-farm operation, followed by a slow decrease afterwards.

Figure 9(a) displays the wind-farm power output, non-dimensionalized with the geostrophic wind speed, for the various LES cases in function of time. In all simulations, the power profile starts with a sharp peak followed by a drop in power output, with a minimum after about 2.5 h of operation. Near the end of the simulation, the power output partly recovers from the initial drop and attains a quasi-steady output level. In this regime, a clear difference in power performance can be observed among the different cases. With respect to the baseline case, we observe that the power output is $13\% \pm 0.2\%$ lower in case S10 (strong inversion) and $20\% \pm 0.3\%$ higher in case S00 (very weak inversion). Comparing the baseline case with cases H10 and H15 shows a monotonic increase in power of $25\% \pm 0.3\%$ and $31\% \pm 0.4\%$ with inversion-layer height. In Figure 9(b), the ratio of wind-farm power output and u_{*hi}^3 is compared for the different cases. After the initial transient, the wind-farm power output appears to scale roughly with u_{*hi}^3 . (The uncertainty on the power averages mentioned above corresponds to the standard deviation on the 10-h average. It was obtained from the root-mean-square of the power, and the square-root of the number of statistically independent samples in our 10-h averaging period. The latter was estimated using an integral time scale of 100 s, leading to approximately 360 independent samples.)

We further investigate the dominating factors that explain this power difference. To this end, the total kinetic-energy budget of the CNBL is discussed. The total kinetic-energy equation (per unit mass) is derived by first multiplying momentum equation (4) with \tilde{u}_i and subsequently averaging the equation over horizontal planes,

$$\begin{aligned} \frac{\partial \langle E_k \rangle}{\partial t} + \frac{\partial}{\partial x_j} \left(\langle \tilde{u}_j \rangle \langle E_k \rangle + \langle \tilde{u}_i \rangle \langle \tilde{u}'_i \tilde{u}'_j \rangle + \frac{1}{2} \langle \tilde{u}'_j \tilde{u}'_i \tilde{u}'_i \rangle + \langle \tilde{u}'_j \tilde{p}^* \rangle + \langle \tilde{u}_i \tau_{ij}^r \rangle \right) \\ = \frac{g}{\theta_0} \langle \tilde{u}_3 (\tilde{\theta} - \theta_0) \rangle + \langle \tau_{ij}^r \frac{\partial \tilde{u}_i}{\partial x_j} \rangle + \langle \tilde{u}_i f_i \rangle + \langle \tilde{u}_i \rangle \left(-\frac{1}{\rho_0} \frac{\partial p_\infty}{\partial x_i} \right), \end{aligned} \quad (24)$$

where $\langle E_k \rangle$ is defined as $\langle \tilde{u}_i \tilde{u}_i \rangle / 2$, and where here $\tilde{u}'_i = \tilde{u}_i - \langle \tilde{u}_i \rangle$. Equation (24) is now integrated over the boundary-layer height $h_1(t)$, where the Leibniz's rule for differentiation under the integral sign is used for the time-dependent term, i.e.,

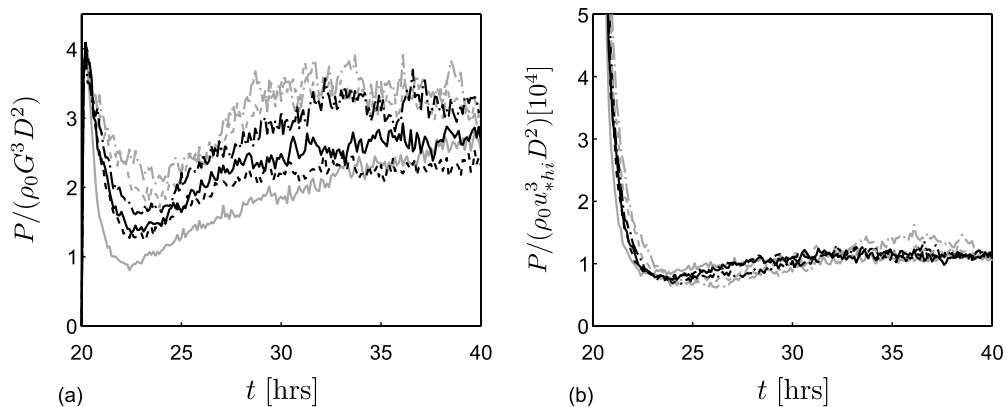


FIG. 9. Total wind-farm power extraction as a function of time, scaled with the geostrophic wind (a) and the friction velocity (b), for the cases REF (solid black line), S10 (dashed black line), S00 (dashed-dotted black line), H02 (solid grey line), H10 (dashed grey line), and H15 (dashed-dotted grey line).

$$\begin{aligned}
\frac{d}{dt} \int_0^{h_1} \langle E_k \rangle dz = & \underbrace{\int_0^{h_1} \frac{g}{\theta_0} \langle \tilde{u}_3 (\tilde{\theta} - \theta_0) \rangle dz}_{\mathcal{P}_{E_p}} + \underbrace{\int_0^{h_1} \langle \tau_{ij}^r \frac{\partial \tilde{u}_i}{\partial x_j} \rangle dz}_{\mathcal{D}} + \underbrace{\int_0^{h_1} \langle \tilde{u}_i f_i \rangle dz}_{\mathcal{P}_F} \\
& + \underbrace{\int_0^{h_1} \langle \tilde{u}_i \rangle \left(-\frac{1}{\rho_0} \frac{\partial p_\infty}{\partial x_i} \right) dz}_{\mathcal{F}} + \underbrace{\langle E_k \rangle \Big|_{h_1}}_{\mathcal{E}} \frac{dh_1}{dt}. \quad (25)
\end{aligned}$$

The term on the left hand side indicates the change in time of the total energy in the boundary layer. The terms on the right hand side include production of potential energy \mathcal{P}_{E_p} , dissipation \mathcal{D} , wind-farm power extraction \mathcal{P}_F , and driving-power term \mathcal{F} . The last term on the right hand side arises due to the time dependence of $h_1(t)$ and corresponds to the amount of energy that is entrained from the free atmosphere due to the growth of the boundary layer. No transport terms arise in Eq. (25) due to the choice of integration limits.

Figure 10(a) shows the energy sources and sinks of total kinetic energy for the baseline case. In the CNBL, the entrainment of kinetic energy is very small but positive, and the production from potential energy is negligible. Further, turbulent dissipation appears to be of the same magnitude as the wind-farm power output throughout the whole simulation. The evolution of the wind-farm power output, the driving-pressure term, and the time-dependent term can be divided into three periods, starting at simulation hours 20, 22.5, and 30, respectively. The first period, i.e., the first two and a half-hours of wind-farm operation, starts with a large peak in wind-farm power output and turbulent dissipation. In this period, the time-dependent term attains a large negative value,

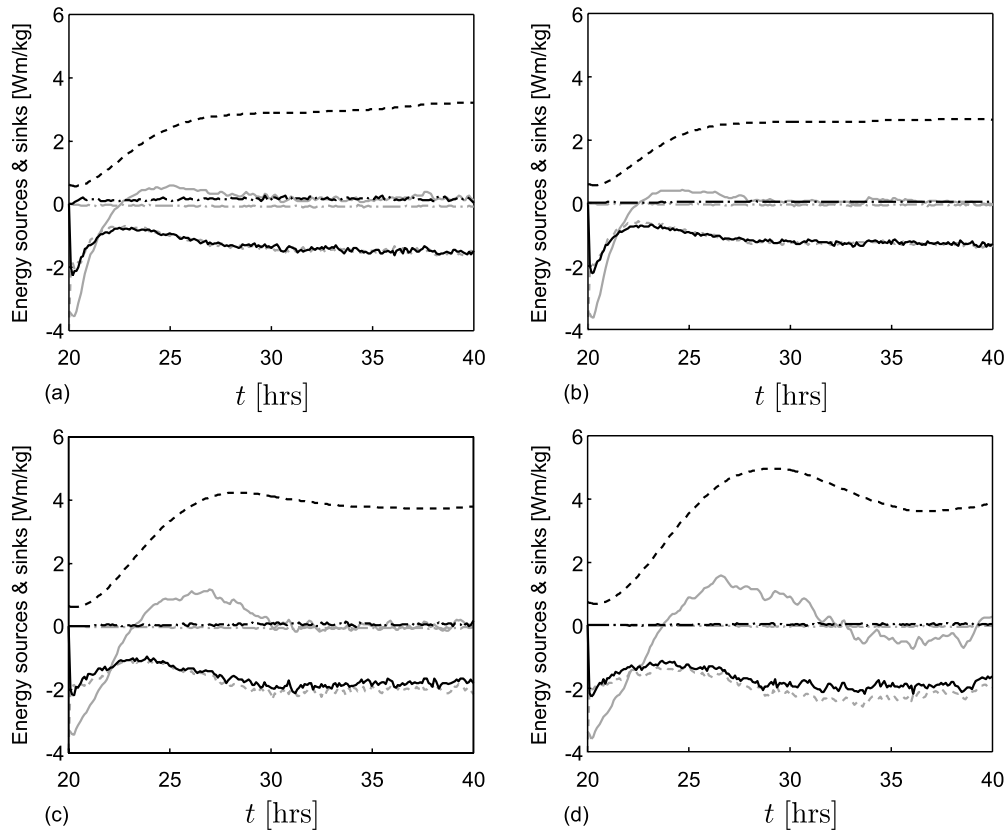


FIG. 10. Energy sources and sinks in the mean kinetic-energy budget as a function of time for cases REF (a), S10 (b), H10 (c), and H15 (d), including wind-farm power extraction \mathcal{P}_F (solid black line), driving power \mathcal{F} (dashed black line), entrainment \mathcal{E} (dashed-dotted black line), time-dependent term (solid grey line), dissipation term \mathcal{D} (dashed grey line), and production of potential energy \mathcal{P}_{E_p} (dashed-dotted grey line).

indicating that the flow is slowed down by the wind farm. Near the end of the first period, the wind-farm power output decreases and the driving-power term increases, both of which reduce the global deceleration of the flow. The second period starts when the wind-farm power output reaches a local minimum. In this period, the energy content of the boundary layer increases again and the wind-farm power recovers slightly. In the last part of the simulation ($t > 30$ h), the time derivative of the mean kinetic energy reaches a steady, slightly positive level, and is almost exactly equal to the energy entrainment. Wind-farm power output, turbulent dissipation, and driving power increase very slowly.

The same trends are observed in Figure 10(b), showing the energy budget terms for case S10, characterized by a higher inversion strength. As the boundary-layer growth of this case is lower than the baseline case (see Figure 8(a)), the energy entrainment is also lower. Similarly, Figures 10(c) and 10(d) show lower energy entrainment rates for the cases H10 and H15. These cases have higher initial inversion layers compared to the baseline case, also leading to slower boundary-layer growth. Overall, the kinetic-energy entrainment is very low in all cases, so this is not explaining the difference in wind-farm power output.

V. A SIMPLE MODEL FOR WIND-FARM POWER EQUILIBRIUM IN QUASI-STEADY CONDITIONS

In the current section, we focus on the power balance in wind farms and derive a simple model that explains the main mechanics for quasi-steady conditions, i.e., conditions where the temporal variation in total boundary-layer energy and vertical entrainment are very small or cancel out. In particular, the dependence of \mathcal{P}_F/G^3 , \mathcal{F}/G^3 , and \mathcal{D}/G^3 on parameters such as Rossby number, boundary layer height, etc., is of interest. As seen in Sec. IV, quasi-steady conditions are obtained after 15–20 h of wind-farm model time. Under these conditions, the power balance is simply governed by $\mathcal{F} = \mathcal{P}_F + \mathcal{D}$, since all other terms can be neglected (cf. Figure 10 and Eq. (25)).

We start from the observation in Figure 9(b) that the wind-farm power extraction scales with u_{*hi}^3 in quasi-steady regime. This can be explained as follows. First of all, the total farm power per farm surface area is given by $\mathcal{P}_F = c'_{ft} \langle \bar{u}^T \rangle_d^3 / 2$, with $c'_{ft} = \pi C'_T / (4s_x s_y)$. Similarly, the total farm thrust force per surface area $\|f_t\| = c'_{ft} \langle \bar{u}^T \rangle_d^2 / 2$. Combining these two equations with Eq. (18) yields

$$\frac{\mathcal{P}_F}{u_{*hi}^3} = (2/c'_{ft})^{1/2} \left(1 + \frac{2u_{*lo}^2}{c'_{ft} \langle \bar{u}^T \rangle_d^2} \right)^{-3/2} = (2/c'_{ft})^{1/2} \left(1 - \frac{u_{*lo}^2}{u_{*hi}^2} \right)^{3/2}. \quad (26)$$

Thus, when $u_{*lo}^2 \ll u_{*hi}^2$, we find $\mathcal{P}_F/u_{*hi}^3 \approx (2/c'_{ft})^{1/2}$, independent of outer-layer parameters such as Rossby number or boundary-layer height, and independent of turbine arrangement pattern. Moreover, in the inner layer, it is logical to assume that $2u_{*lo}^2/(c'_{ft} \langle \bar{u}^T \rangle_d^2)$ is not influenced by outer layer scales. In our LES data, we find that $2u_{*lo}^2/(c'_{ft} \langle \bar{u}^T \rangle_d^2)$ is nearly constant over the various cases and equals 0.135. Thus, we find that this value is not influenced by outer-layer scales even when the wind turbines are located well above the inner layer. To further confirm this for another arrangement pattern, we performed three additional simulations with a staggered wind farm, using the same turbine density and c'_{ft} as for the aligned case, and further equivalent to cases REF, S10, and H10. For these cases, $2u_{*lo}^2/(c'_{ft} \langle \bar{u}^T \rangle_d^2) = 0.124$ is found, which is very close to the aligned case. The difference in \mathcal{P}_F/u_{*hi}^3 between the staggered and aligned wind-farm layout is less than 3%, which follows directly from Eq. (26). Hints of this near independence in fully developed conditions are also observed in field experiments, e.g., in the well documented Horns Rev farm, typical efficiency loss is roughly $(40 \pm 5)\%$ in the last rows of the farm, independent of wind direction (and thus turbine arrangement pattern).^{64,65} Finally, given above scaling for \mathcal{P}_F , it follows that

$$\frac{\mathcal{P}_F}{G^3} = \frac{\mathcal{P}_F}{u_{*hi}^3} C_g^3 \approx (2/c'_{ft})^{1/2} C_g^3, \quad (27)$$

with $C_g \equiv u_{*hi}/G$ the geostrophic drag (cf. further below). Note that the approximation in Eq. (27) is not valid for $c'_{ft} \rightarrow 0$, as in that case $u_{*lo}^2 \rightarrow u_{*hi}^2$.

The driving power \mathcal{F} in the boundary layer can also be further elaborated. Similar to Zilitinkevich,⁵⁶ it can be reformulated using the horizontally averaged and integrated momentum equations for \tilde{u}_1 and \tilde{u}_2 , Eq. (4) (assuming steady state),

$$-\int_0^\infty f_c G \sin \alpha + \int_0^\infty f_c \langle \tilde{u}_2 \rangle dz = -\tau_{w1} - \int_0^\infty \langle \mathbf{f} \cdot \mathbf{e}_1 \rangle dz, \quad (28)$$

$$\int_0^\infty f_c G \cos \alpha - \int_0^\infty f_c \langle \tilde{u}_1 \rangle dz = -\tau_{w2}. \quad (29)$$

Using Eqs. (18), (28), and (29), the driving-power term \mathcal{F} can be written as

$$\mathcal{F} = \int_0^\infty f_c G (\langle \tilde{u}_2 \rangle \cos \alpha - \langle \tilde{u}_1 \rangle \sin \alpha) dz \quad (30)$$

$$= G \cos \alpha \left(-\tau_{w1} - \int_0^\infty \langle \mathbf{f}_t \cdot \mathbf{e}_1 \rangle dz \right) - G \sin \alpha \tau_{w2} \quad (31)$$

$$= G \cos(\alpha - \alpha_*) u_{*hi}^2, \quad (32)$$

where α_* is the angle between $-(\boldsymbol{\tau}_w + \mathbf{f}_t)$ and the x -coordinate. This angle remains small for all cases, i.e., ranging between -4° and 4° . Hence, neglecting α_* , the ratio of the driving-power term and u_{*hi}^3 is given by

$$\frac{\mathcal{F}}{u_{*hi}^3} \approx \frac{G \cos \alpha}{u_{*hi}} = \frac{1}{\kappa} \ln \left(\frac{C_g Ro_h}{\bar{z}_{0,hi}} \right) - F_1(C_g, Ro_h, \bar{h}), \quad (33)$$

with $Ro_h = G/f_c z_h$ the Rossby number based on the turbine hub height,⁶⁶ $\bar{z}_{0,hi} = z_{0,hi}/z_h$ the non-dimensional surface roughness, and $\bar{h} = h/z_h$ the non-dimensional boundary-layer height (for which we use the measure h_1/z_h). The second equality in Eq. (33) follows from the classical resistance law for the matched layer,²⁵ where F_1 is usually considered constant. However, as postulated by Csanady,¹⁶ amongst others,^{17,23,67} F_1 is a function of outer-layer parameters. Explicit expressions for $F_1(C_g, Ro_h, \bar{h})$ can be derived by solving the Ekman-layer equations and using, e.g., constant,¹⁶ quadratic,⁶⁷ or cubic⁶⁷ eddy-viscosity profiles in the outer layer of the ABL to express the shear stresses (cf. the Appendix for details). Further, the wind farm-induced surface roughness $z_{0,hi}$ is used in the resistance law, as suggested by Meyers and Meneveau.⁶⁶ This surface roughness can be computed from the LES velocity profiles or may be estimated using an effective surface roughness model.^{1,4,61} Finally, normalized with respect to the geostrophic wind, we find

$$\frac{\mathcal{F}}{G^3} = \left[\frac{1}{\kappa} \ln \left(\frac{C_g Ro_h}{\bar{z}_{0,hi}} \right) - F_1(C_g, Ro_h, \bar{h}) \right] C_g^3. \quad (34)$$

An expression for C_g follows from $G \sin \alpha / u_{*hi} = -F_2(C_g, Ro_h, \bar{h})$ (cf. the Appendix for details) in combination with Eq. (33), yielding

$$\frac{1}{C_g^2} = [F_2(C_g, Ro_h, \bar{h})]^2 + \left[\frac{1}{\kappa} \ln \left(\frac{C_g Ro_h}{\bar{z}_{0,hi}} \right) - F_1(C_g, Ro_h, \bar{h}) \right]^2. \quad (35)$$

Thus, in summary, Eqs. (27), (34), and (35), together with expressions for F_1 and F_2 , form a closed analytical model that allows to express \mathcal{P}_F/G^3 and \mathcal{F}/G^3 .

Figure 11 shows the wind-farm power extraction \mathcal{P}_F/G^3 and the driving power \mathcal{F}/G^3 as a function of the dimensionless boundary-layer height \bar{h} and the geostrophic drag C_g . Data from the LES cases have been averaged over the last 10 simulation hours and are shown with symbols. For the analytical model, we used a cubic eddy-viscosity profile⁶⁷ (cf. the Appendix), and fitted the model to LES data using the von Kármán constant as fitting parameter, yielding $\kappa = 0.43$. Further, \mathcal{P}_F/u_{*hi}^3 and the wind farm-induced surface roughness $\bar{z}_{0,hi}$ were estimated from LES data to be 6.4 and 0.0223, respectively. The analytical model matches good with the LES results. We observe that the wind-farm power extraction \mathcal{P}_F/G^3 and the driving power \mathcal{F}/G^3 are monotonous increasing functions of the boundary-layer height. The driving power \mathcal{F}/G^3 increases faster since $\cos \alpha$ increases faster than C_g . From this figure, we conclude that the difference in wind-farm power

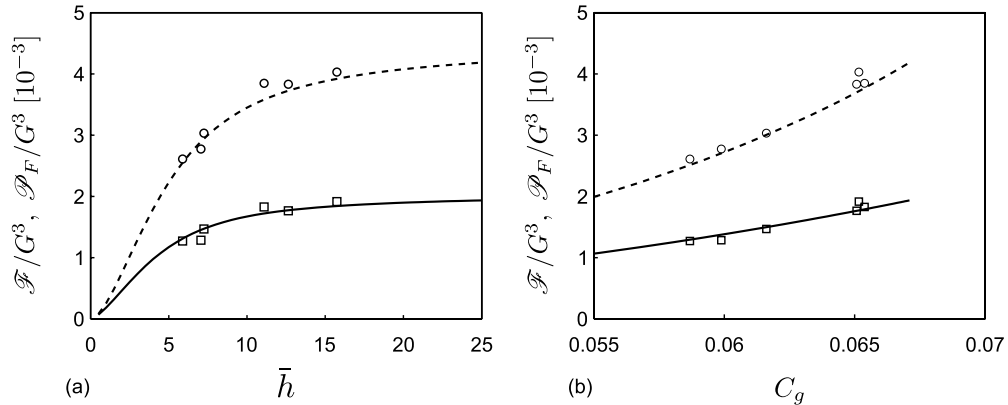


FIG. 11. Wind-farm power extraction \mathcal{P}_F/G^3 (solid line) and driving power \mathcal{F}/G^3 (dashed line) as a function of (a) dimensionless BL height \bar{h} and (b) geostrophic drag C_g , obtained from the presented power model governed by Eqs. (27), (34), and (35), using a cubic eddy-viscosity profile⁶⁷ with $\kappa = 0.43$. LES results averaged over the last ten simulation hours show \mathcal{P}_F/G^3 (squares) and \mathcal{F}/G^3 (circles).

extraction between the LES cases REF, H02, H10, and H15 is directly caused by the difference in initial inversion layer height, whereas the difference between the cases REF, S10, and S00 is only indirectly caused by the varying inversion strength through its effect on the entrainment rate of the boundary layer.

VI. CONCLUSION

This study aimed at determining the behaviour of an infinite wind-turbine array located in a conventionally neutral atmospheric boundary layer. Such a CNBL is often capped by a strong temperature inversion layer, which limits vertical entrainment of kinetic energy in the boundary layer, and thus potentially reduces the energy available for power extraction by the wind turbines.

Large eddy simulations were used to study the performance of a wind farm under capping inversions with varying strengths and heights, and the limit of an infinite wind-turbine array was used, allowing for periodic boundary conditions in the simulations, similar to the approach followed by Calaf *et al.*⁴ for a pressure-driven boundary layer. In order to obtain a CNBL with the required capping-inversion structure, special attention was paid to the initial conditions of the different simulations. In addition, a wind angle controller was implemented to ensure that the wind at the hub height of the turbines was directed along the x-axis. In this way, the wind-farm geometrical pattern was independent of the geostrophic angle and identical for all simulations.

LES results of the CNBL with wind turbines revealed some essential differences between the current approach and the frequently used neutral pressure-driven boundary layers. For instance, the double log layer in the mean velocity profile does not reach up to the top of the domain in the CNBL, and the expected shear stress deviates from the well-known linear profile near the inversion. Further, it was observed that the direction of the flow changes with height, and a sharp change in wind direction was observed inside the inversion layer.

Comparison of the various LES cases showed that the strength and the height of the capping inversion have a strong influence on the boundary-layer flow. For example, the growth rate of the wind-farm boundary layer was shown to decrease with increasing inversion strength or height. Moreover, in the presence of a capping inversion, only modest boundary-layer growth rates were observed. In contrast, the boundary-layer growth in absence of an inversion was about three times the growth rate of the baseline case. The geostrophic angle also decreased for increasing inversion height.

For the simulations in this study, it was observed that the power extraction by the wind farm depends on the height and strength of the inversion layer. Increasing the strength of the inversion layer from 2.5 to 10 K resulted in a $13\% \pm 0.2\%$ decrease in wind-farm power output. On the

other hand, starting the simulation without an inversion layer resulted in a $20\% \pm 0.3\%$ increase compared to the 2.5 K baseline case. The height of the inversion base had an even bigger influence on the power output, resulting in an increase of up to $31\% \pm 0.4\%$. A detailed analysis of the mean kinetic-energy balance illustrated that the variation in power extraction between these different cases mainly originates from the work done by the driving pressure gradient related to the boundary-layer height and the geostrophic angle, while entrainment of kinetic energy from the free atmosphere did not play a significant role. Furthermore, it was found that the variation in power extraction for different inversion strengths is energetically not related to different amounts of energy entrained, but explained by a difference in boundary layer growth, leading to higher boundary layers for lower inversion strengths.

Based on the observation that the wind-farm power extraction scales with the friction velocity cubed, a simple analytical model was developed that allows to obtain wind-farm power output and driving power for the fully developed regime as function of Rossby number, and boundary layer height. From this model, it was shown that the wind-farm power extraction and the work done by the driving pressure gradient are monotonous increasing functions of boundary layer height and geostrophic drag, but driving power increases faster due to the effect of the geostrophic angle.

In the current work, it was shown that the definition of a steady state in a wind-farm CNBL regime may only be possible after several hours of simulation. Even then, the boundary layer slowly evolves, and a true equilibrium state can only emerge after very long simulation times, with a capping inversion that has risen above the asymptotic equilibrium height of the CNBL. In practice, the CNBL may not exist that long in real atmospheric conditions, in which the absence of positive or negative heat fluxes at the ground surface is often limited in time. Moreover, also the limit of infinite wind-farm boundary layers remains a theoretical framework, that, e.g., does not include effects of internal boundary-layer development in finite wind farms. In view of the large impact of capping-inversion parameters on wind-farm CNBLs, we believe that research into CNBL transition effects on finite wind farms subject to various inversion parameters is an important topic for further research.

ACKNOWLEDGMENTS

The authors acknowledge support from the European Research Council (FP7-Ideas, Grant No. 306471). The computational resources and services used in this work were provided by the VSC (Flemish Supercomputer Center), funded by the Hercules Foundation and the Flemish Government–department EWI.

APPENDIX: EXPLICIT EXPRESSIONS FOR $F_1(C_g, Ro_h, \bar{h})$ AND $F_2(C_g, Ro_h, \bar{h})$

By matching the law of the wall with the velocity-defect law in the surface layer, it can be shown that $F_1(C_g, Ro_h, \bar{h})$ and $F_2(C_g, Ro_h, \bar{h})$ are given by²⁵

$$F_1(C_g, Ro_h, \bar{h}) = \frac{U - U_g}{u_{*hi}} - \frac{1}{\kappa} \ln \left(\frac{\eta \bar{h}}{C_g Ro_h} \right), \quad (\text{A1})$$

$$F_2(C_g, Ro_h, \bar{h}) = -\frac{V_g}{u_{*hi}}, \quad (\text{A2})$$

using $V \approx 0$ in the surface layer. Further, $U_g = G \cos \alpha$, $V_g = G \sin \alpha$, and $\eta = z/h$. The velocity defect can be found by solving the so-called Ekman-layer equations, which hold for a stationary, horizontally homogeneous atmospheric boundary layer,²⁵

$$-f_c (V - V_g) = \frac{\partial \tau_{xz}}{\partial z}, \quad (\text{A3})$$

$$f_c (U - U_g) = \frac{\partial \tau_{yz}}{\partial z}, \quad (\text{A4})$$

where use has been made of geostrophic balance (1). These equations can be closed using gradient transfer theory: $(\tau_{xz}, \tau_{yz}) = \nu_T(\partial U/\partial z, \partial V/\partial z)$, with ν_T the eddy viscosity. Non-dimensionalizing equations (A3) and (A4) and writing them in complex notation yield a second order complex differential equation for the velocity defect vector $w_d = (U - U_g)/u_{*hi} + i(V - V_g)/u_{*hi}$,

$$\frac{d^2 w_d}{d\eta^2} - i \frac{\bar{h}}{C_g Ro_h} \frac{w_d}{K} = 0, \quad (\text{A5})$$

with $K(\eta) = \nu_T/u_{*hi}h$ a non-dimensional eddy viscosity.

In the literature, closed-form solutions to Eq. (A5) are found for some specific eddy viscosity profiles. Csanady¹⁶ found a solution assuming a constant eddy viscosity

$$w_d = (i - 1) \left(\frac{C_g Ro_h}{2K\bar{h}} \right)^{1/2} \frac{\cosh[\gamma(\eta - 1)]}{\sinh(\gamma)}, \quad (\text{A6})$$

with $\gamma = (i + 1)(2KC_g Ro_h/\bar{h})^{-1/2}$. Inserting (A6) in Eqs. (A1) and (A2) yields

$$F_1(C_g, Ro_h, \bar{h}) = -\frac{1}{\kappa} \ln \left(\frac{\eta_s \bar{h}}{C_g Ro_h} \right) + \text{Re} \{w_d(\eta_s)\}, \quad (\text{A7})$$

$$F_2(C_g, Ro_h, \bar{h}) = \text{Im} \{w_d(0)\}, \quad (\text{A8})$$

where $\eta_s = h_s/h$, with h_s the top of the surface layer (i.e., the location where inner and outer profiles are matched).

Nieuwstadt⁶⁷ provided solutions to Eq. (A5) for a quadratic profile, i.e., $K_I = \kappa\eta(1 - \eta)$, and a cubic profile, i.e., $K_{II} = \kappa\eta(1 - \eta)^2$,

$$w_{d,I} = -\frac{1}{\kappa} \frac{\pi}{\cos \pi\beta} {}_2F_1\left(\frac{1}{2} + \beta, \frac{1}{2} - \beta; 1; 1 - \eta\right), \quad (\text{A9})$$

$$w_{d,II} = \frac{1}{\kappa} i \frac{\alpha^2 \Gamma^2(\alpha)}{C\Gamma(2\alpha)} (1 - \eta)^{\alpha-1} {}_2F_1(\alpha + 1, \alpha - 1; 2\alpha; 1 - \eta), \quad (\text{A10})$$

where

$$\beta = \frac{1}{2} \sqrt{1 - 4iC}, \quad \alpha = \frac{1}{2} + \frac{1}{2} \sqrt{1 + 4iC}, \quad \text{and} \quad C = \frac{\bar{h}}{\kappa C_g Ro_h}. \quad (\text{A11})$$

In these expressions, $\Gamma(x)$ is the gamma function and ${}_2F_1(a, b; c; x)$ is the hypergeometric function. Nieuwstadt also derives an expression for $F_1(C_g, Ro_h, \bar{h})$ and $F_2(C_g, Ro_h, \bar{h})$ by taking the limit of Eqs. (A9) and (A10) for $z \rightarrow 0$ and matching it to a surface-layer profile. This gives for the quadratic profile

$$F_1(C_g, Ro_h, \bar{h}) = -\frac{1}{\kappa} \ln \left(\frac{\bar{h}}{C_g Ro_h} \right) + \frac{1}{\kappa} \text{Re} \left\{ \psi\left(\frac{1}{2} - \beta\right) + \psi\left(\frac{1}{2} + \beta\right) - 2\psi(1) \right\}, \quad (\text{A12})$$

$$F_2(C_g, Ro_h, \bar{h}) = \frac{1}{\kappa} \text{Im} \left\{ \psi\left(\frac{1}{2} - \beta\right) + \psi\left(\frac{1}{2} + \beta\right) - 2\psi(1) \right\} \quad (\text{A13})$$

and for the cubic profile

$$F_1(C_g, Ro_h, \bar{h}) = -\frac{1}{\kappa} \ln \left(\frac{\bar{h}}{C_g Ro_h} \right) + \frac{1}{\kappa} \text{Re} \left\{ \psi(\alpha + 1) + \psi(\alpha - 1) - 2\psi(1) \right\}, \quad (\text{A14})$$

$$F_2(C_g, Ro_h, \bar{h}) = \frac{1}{\kappa} \text{Im} \left\{ \psi(\alpha + 1) + \psi(\alpha - 1) - 2\psi(1) \right\}, \quad (\text{A15})$$

with $\psi(x)$ the psi-function or digamma function.

¹ S. Frandsen, R. Barthelmie, S. Pryor, O. Rathmann, S. Larsen, J. Højstrup, and M. Thøgersen, "Analytical modelling of wind speed deficit in large offshore wind farms," *Wind Energy* **9**(1-2), 39–53 (2006).

² S. Wharton and J. K. Lundquist, "Atmospheric stability affects wind turbine power collection," *Environ. Res. Lett.* **7**(1), 014005 (2012).

- ³ K. S. Hansen, R. Barthelmie, L. E. Jensen, and A. Sommer, "The impact of turbulence intensity and atmospheric stability on power deficits due to wind turbine wakes at horns rev wind farm," *Wind Energy* **15**(1), 183–196 (2012).
- ⁴ M. Calaf, C. Meneveau, and J. Meyers, "Large eddy simulation study of fully developed wind-turbine array boundary layers," *Phys. Fluids* **22**, 015110 (2010).
- ⁵ R. Johnstone and G. N. Coleman, "The turbulent ekman boundary layer over an infinite wind-turbine array," *J. Wind Eng. Ind. Aerodyn.* **100**(1), 46–57 (2012).
- ⁶ H. Lu and F. Porté-Agel, "Large-eddy simulation of a very large wind farm in a stable atmospheric boundary layer," *Phys. Fluids* **23**(6), 065101 (2011).
- ⁷ M. Abkar and F. Porté-Agel, "The effect of free-atmosphere stratification on boundary-layer flow and power output from very large wind farms," *Energies* **6**(5), 2338–2361 (2013).
- ⁸ M. Abkar and F. Porté-Agel, "Mean and turbulent kinetic energy budgets inside and above very large wind farms under conventionally-neutral condition," *Renewable Energy* **70**(0), 142–152 (2014).
- ⁹ C. Hasager, A. Peña, T. Mikkelsen, S.-E. Gryning, M. Courtney, and P. B. Sørensen, 12MW: Final report, Report No. Risø-R-1690(EN), June 2009.
- ¹⁰ A. Andren, A. R. Brown, P. J. Mason, J. Graf, U. Schumann, C.-H. Moeng, and F. T. M. Nieuwstadt, "Large-eddy simulation of a neutrally stratified boundary layer: A comparison of four computer codes," *Q. J. R. Meteorol. Soc.* **120**(520), 1457–1484 (1994).
- ¹¹ G. D. Hess and J. R. Garratt, "Evaluating models of the neutral, barotropic planetary boundary layer using integral measures: Part I. Overview," *Boundary Layer Meteorol.* **104**(3), 333–358 (2002).
- ¹² G. D. Hess and J. R. Garratt, "Evaluating models of the neutral, barotropic planetary boundary layer using integral measures: Part II. Modelling observed conditions," *Boundary Layer Meteorol.* **104**(3), 359–369 (2002).
- ¹³ P. J. Mason, "Large-eddy simulation of the convective atmospheric boundary layer," *J. Atmos. Sci.* **46**(11), 1492–1516 (1989).
- ¹⁴ C.-H. Moeng and P. P. Sullivan, "A comparison of shear- and buoyancy-driven planetary boundary layer flows," *J. Atmos. Sci.* **51**(7), 999–1022 (1994).
- ¹⁵ R. J. Beare, M. K. Macvean, A. A. M. Holtslag, J. Cuxart, I. Esau, J.-C. Golaz, M. A. Jimenez, M. Khairoutdinov, B. Kosović, D. Lewellen, T. S. Lund, J. K. Lundquist, A. McCabe, A. F. Moene, Y. Noh, S. Raasch, and P. P. Sullivan, "An intercomparison of large-eddy simulations of the stable boundary layer," *Boundary Layer Meteorol.* **118**(2), 247–272 (2006).
- ¹⁶ G. T. Csanady, "Equilibrium theory of the planetary boundary layer with an inversion lid," *Boundary Layer Meteorol.* **6**(1-2), 63–79 (1974).
- ¹⁷ S. S. Zilitinkevich and I. N. Esau, "On integral measures of the neutral barotropic planetary boundary layer," *Boundary-Layer Meteorol.* **104**(3), 371–379 (2002).
- ¹⁸ J. C. McWilliams, P. C. Gallacher, C.-H. Moeng, and J. C. Wyngaard, "Modeling the oceanic planetary boundary layer," in *Large-Eddy Simulations of Complex Engineering and Geophysical Flows*, edited by B. Galperin and S. A. Orszag (Cambridge University Press, 1993), pp. 441–454.
- ¹⁹ P. P. Sullivan, J. C. McWilliams, and C.-H. Moeng, "A subgrid-scale model for large-eddy simulation of planetary boundary-layer flows," *Boundary Layer Meteorol.* **71**(3), 247–276 (1994).
- ²⁰ C.-L. Lin, C.-H. Moeng, P. P. Sullivan, and J. C. McWilliams, "The effect of surface roughness on flow structures in a neutrally stratified planetary boundary layer flow," *Phys. Fluids* **9**(11), 3235–3249 (1997).
- ²¹ I. N. Esau, "Parameterization of a surface drag coefficient in conventionally neutral planetary boundary layer," *Ann. Geophys.* **22**(10), 3353–3362 (2004).
- ²² J. R. Taylor and S. Sarkar, "Direct and large eddy simulations of a bottom ekman layer under an external stratification," in *The Fifth International Symposium on Turbulence and Shear Flow Phenomena (TSFP5)*, *Int. J. Heat Fluid Flow* **29**(3), 721–732 (2008).
- ²³ G. D. Hess, "The neutral, barotropic planetary boundary layer, capped by a low-level inversion," *Boundary Layer Meteorol.* **110**(3), 319–355 (2004).
- ²⁴ Z. Sorbjan, "Effects caused by varying the strength of the capping inversion based on a large eddy simulation model of the shear-free convective boundary layer," *J. Atmos. Sci.* **53**(14), 2015–2024 (1996).
- ²⁵ H. Tennekes and J. L. Lumley, *A First Course in Turbulence* (MIT Press, 1972).
- ²⁶ R. B. Stull, *An Introduction to Boundary Layer Meteorology* (Springer, 1988).
- ²⁷ S. P. S. Arya, "Comments on similarity theory for the planetary boundary layer of time-dependent height," *J. Atmos. Sci.* **32**(4), 839–840 (1975).
- ²⁸ S. P. S. Arya, "Comparative effects of stability, baroclinity and the scale-height ratio on drag laws for the atmospheric boundary layer," *J. Atmos. Sci.* **35**(1), 40–46 (1978).
- ²⁹ D. K. Lilly, "Models of cloud-topped mixed layers under a strong inversion," *Q. J. R. Meteorol. Soc.* **94**(401), 292–309 (1968).
- ³⁰ M. Tjernström and A.-S. Smedman, "The vertical turbulence structure of the coastal marine atmospheric boundary layer," *J. Geophys. Res.: Oceans* **98**(C3), 4809–4826, doi:10.1029/92JC02610 (1993).
- ³¹ G. J. Steeneveld, B. J. H. van de Wiel, and A. A. M. Holtslag, "Comments on deriving the equilibrium height of the stable boundary layer," *Q. J. R. Meteorol. Soc.* **133**(622), 261–264 (2007).
- ³² S. S. Zilitinkevich, I. N. Esau, and A. Baklanov, "Further comments on the equilibrium height of neutral and stable planetary boundary layers," *Q. J. R. Meteorol. Soc.* **133**(622), 265–271 (2007).
- ³³ H. Tennekes, "A model for the dynamics of the inversion above a convective boundary layer," *J. Atmos. Sci.* **30**(4), 558–567 (1973).
- ³⁴ J. A. Businger and H. Charnock, "Boundary layer structure in relation to larger-scale flow: Some remarks on the jasin observations," *Philos. Trans. R. Soc., A* **308**(1503), 445–449 (1983).
- ³⁵ R. A. Brost, D. H. Lenschow, and J. C. Wyngaard, "Marine stratocumulus layers. Part I: Mean conditions," *J. Atmos. Sci.* **39**(4), 800–817 (1982).

- ³⁶ S. Nicholls, "Aircraft observations of the ekman layer during the joint air-sea interaction experiment," *Q. J. R. Meteorol. Soc.* **111**(468), 391–426 (1985).
- ³⁷ A. L. M. Grant, "Observations of boundary layer structure made during the 1981 kontur experiment," *Q. J. R. Meteorol. Soc.* **112**(473), 825–841 (1986).
- ³⁸ C.-H. Moeng, "A large-eddy-simulation model for the study of planetary boundary-layer turbulence," *J. Atmos. Sci.* **41**(13), 2052–2062 (1984).
- ³⁹ E. Bou-Zeid, C. Meneveau, and M. Parlange, "A scale-dependent lagrangian dynamic model for large eddy simulation of complex turbulent flows," *Phys. Fluids* **17**(2), 025105 (2005).
- ⁴⁰ B. Stevens, C.-H. Moeng, and P. P. Sullivan, "Entrainment and subgrid lengthscales in large-eddy simulations of atmospheric boundary-layer flows," *IUTAM Symposium on Developments in Geophysical Turbulence*, Fluid Mechanics and Its Applications Vol. 58, edited by R. M. Kerr and Y. Kimura (Springer, Netherlands, 2000), pp. 253–269.
- ⁴¹ P. J. Mason and D. J. Thomson, "Stochastic backscatter in large-eddy simulations of boundary layers," *J. Fluid Mech.* **242**, 51–78 (1992).
- ⁴² A. Jimenez, A. Crespo, E. Migoya, and J. Garcia, "Advances in large-eddy simulation of a wind turbine wake," *J. Phys.: Conf. Ser.* **75**(1), 012041 (2007).
- ⁴³ A. Jimenez, A. Crespo, E. Migoya, and J. Garcia, "Large-eddy simulation of spectral coherence in a wind turbine wake," *Environ. Res. Lett.* **3**(1), 015004 (2008).
- ⁴⁴ J. Meyers and C. Meneveau, "Large eddy simulations of large wind-turbine arrays in the atmospheric boundary layer," AIAA Paper 2010-827, 2010.
- ⁴⁵ J. Meyers and C. Meneveau, "Flow visualization using momentum and energy transport tubes and applications to turbulent flow in wind farms," *J. Fluid Mech.* **715**, 335–358 (2013).
- ⁴⁶ Y.-T. Wu and F. Porté-Agel, "Large-eddy simulation of wind-turbine wakes: Evaluation of turbine parametrisations," *Boundary Layer Meteorol.* **138**(3), 345–366 (2011).
- ⁴⁷ A. Sescu and C. Meneveau, "A control algorithm for statistically stationary large-eddy simulations of thermally stratified boundary layers," *Q. J. R. Meteorol. Soc.* **140**(683), 2017–2022 (2014).
- ⁴⁸ C. Canuto, M. Y. Hussaini, A. Quarteroni, and T. A. Zang, *Spectral Methods in Fluid Dynamics* (Springer-Verlag, Berlin, 1988).
- ⁴⁹ R. W. C. P. Verstappen and A. E. P. Veldman, "Symmetry-preserving discretization of turbulent flow," *J. Comput. Phys.* **187**(1), 343–368 (2003).
- ⁵⁰ E. Lindborg, "The energy cascade in a strongly stratified fluid," *J. Fluid Mech.* **550**, 207–242 (2006).
- ⁵¹ G. Brethouwer, P. Billant, E. Lindborg, and J.-M. Chomza, "Scaling analysis and simulation of strongly stratified turbulent flows," *J. Fluid Mech.* **585**, 343–368 (2007).
- ⁵² M. L. Waite, "Stratified turbulence at the buoyancy scale," *Phys. Fluids* **23**(6), 066602 (2011).
- ⁵³ S. Khani and M. L. Waite, "Buoyancy scale effects in large-eddy simulations of stratified turbulence," *J. Fluid Mech.* **754**, 75–97 (2014).
- ⁵⁴ P. P. Sullivan, J. B. Edson, T. Hristov, and J. C. McWilliams, "Large-eddy simulations and observations of atmospheric marine boundary layers above nonequilibrium surface waves," *J. Atmos. Sci.* **65**(4), 1225–1245 (2008).
- ⁵⁵ G. Rampanelli and D. Zardi, "A method to determine the capping inversion of the convective boundary layer," *J. Appl. Meteorol.* **43**(6), 925–933 (2004).
- ⁵⁶ S. S. Zilitinkevich, "Velocity profiles, the resistance law and the dissipation rate of mean flow kinetic energy in a neutrally and stably stratified planetary boundary layer," *Boundary Layer Meteorol.* **46**(4), 367–387 (1989).
- ⁵⁷ J. S. Schröter, A. F. Moene, and A. A. M. Holtslag, "Convective boundary layer wind dynamics and inertial oscillations: The influence of surface stress," *Q. J. R. Meteorol. Soc.* **139**(676), 1694–1711 (2013).
- ⁵⁸ B. Kosović and J. A. Curry, "A large eddy simulation study of a quasi-steady, stably stratified atmospheric boundary layer," *J. Atmos. Sci.* **57**(8), 1052–1068 (2000).
- ⁵⁹ J. W. Deardorff, "Prediction of convective mixed-layer entrainment for realistic capping inversion structure," *J. Atmos. Sci.* **36**(3), 424–436 (1979).
- ⁶⁰ M. C. VanZanten, P. G. Duynkerke, and J. W. M. Cuijpers, "Entrainment parameterization in convective boundary layers," *J. Atmos. Sci.* **56**(6), 813–828 (1999).
- ⁶¹ S. Frandsen, "On the wind speed reduction in the center of large clusters of wind turbines," *J. Wind Eng. Ind. Aerodyn.* **39**(1-3), 251–265 (1992).
- ⁶² M. Calaf, M. B. Parlange, and C. Meneveau, "Large eddy simulation study of scalar transport in fully developed wind-turbine array boundary layers," *Phys. Fluids* **23**(12), 126603 (2011).
- ⁶³ M. R. Raupach, R. A. Antonia, and S. Rajagopalan, "Rough-wall turbulent boundary layers," *Appl. Mech. Rev.* **44**(1), 1–25 (1991).
- ⁶⁴ R. J. Barthelmie, O. Rathmann, S. T. Frandsen, K. S. Hansen, E. Politis, J. Prospathopoulos, K. Rados, D. Cabezon, W. Schlez, J. Phillips, A. Neubert, J. G. Schepers, and S. P. van der Pijl, "Modelling and measurements of wakes in large wind farms," *J. Phys.: Conf. Ser.* **75**(1), 012049 (2007).
- ⁶⁵ R. J. Barthelmie, K. Hansen, S. T. Frandsen, O. Rathmann, J. G. Schepers, W. Schlez, J. Phillips, K. Rados, A. Zervos, E. S. Politis, and P. K. Chaviaropoulos, "Modelling and measuring flow and wind turbine wakes in large wind farms offshore," *Wind Energy* **12**(5), 431–444 (2009).
- ⁶⁶ J. Meyers and C. Meneveau, "Optimal turbine spacing in fully developed wind farm boundary layers," *Wind Energy* **15**(2), 305–317 (2012).
- ⁶⁷ F. T. M. Nieuwstadt, "On the solution of the stationary, baroclinic Ekman-layer equations with a finite boundary-layer height," *Boundary Layer Meteorol.* **26**(4), 377–390 (1983).